# Photoionization microscopy of hydrogen atom near a metal surface*

Yang Hai-Feng(杨海峰), Wang Lei(汪 磊), Liu Xiao-Jun(柳晓军), and Liu Hong-Ping(刘红平)†

*State Key Laboratory of Magnetic Resonance and Atomic and Molecular Physics, Wuhan Institute of Physics and Mathematics, Chinese Academy of Sciences, Wuhan* 430071, *China*

(Received 14 December 2010; revised manuscript received 11 January 2011)

We have studied the ionization of Rydberg hydrogen atom near a metal surface with a semiclassical analysis of photoionization microscopy. Interference patterns of the electron radial distribution are calculated at different scaled energies above the classical saddle point and at various atom–surface distances. We find that different types of trajectories contribute predominantly to different manifolds in a certain interference pattern. As the scaled energy increases, the structure of the interference pattern evolves smoothly and more types of trajectories emerge. As the atom approaches the metal surface closer, there are more types of trajectories contributing to the interference pattern as well. When the Rydberg atom comes very close to the metal surface or the scaled energy approaches the zero field ionization energy, the potential induced by the metal surface will make atomic system chaotic. The results also show that atoms near a metal surface exhibit similar properties like the atoms in the parallel electric and magnetic fields.

**Keywords:** photoionization microscopy, interaction of atom with surface, semiclassical theory

**PACS:** 32.80.Fb, 34.35.+a, 03.65.Sq **DOI:** 10.1088/1674-1056/20/6/063203

## 1. Introduction

Microscopy is a kind of photoelectron imaging, by which we can directly observe the oscillatory structure of a wave function in a macroscopic scale.[1] The image recorded on the detector is the square modulus of the transverse component of the photo-electronic wave function in the process of photodetachment or photoionization. In the early 1980s, Demkov,[2] Kondratovich and Ostrovsk[3,4] introduced the principle of photodetachment and photoionization microscopy. They studied the microscopy theoretically and discussed the possibility of an experiment on photodetachment or photoionization process in the presence of an electric field. As a powerful technique to investigate electron dynamics, microscopy has been used to study the photodetachment and photoionization of atoms in an electric field or parallel electric and magnetic fields for many years.

Photodetachment microscopy in an electric field as well as in parallel fields is simple enough to permit analytic quantum and semiclassical solutions. Blondel *et al*. first applied photodetachment microscopy to $Br^-$ in electric fields experimentally[5] and then to $O^-$.[6] Theoretically, the quantum calculation performed by Kramer *et al*.[7] agreed well with the experimental results presented by Blondel *et al*.[5] Before the experiment of Blondel *et al*., Du had developed a semiclassical method to predict outgoing electron current distributions in photodetachment of $H^-$ in electric fields.[8] As to the atom in parallel electric and magnetic fields, quantum and semiclassical calculations are performed to investigate the photodetachment dynamics of the electron.[9−11]

Rather than the photodetachment microscopy, many works have been done to study the photoionization process in the presence of an electric field using a position-sensitive detector.[12−15] In the photoionization, the escaping electron is affected by the long-range Coulomb field of the residual ion as well and the photoionization microscopy can give more complex observable interference patterns. Nicole *et al*. realized photoionization microscopy experimentally for the first time and observed the transverse component of the electronic wave function of Xe.[14] They found that the structure of the interference pattern evolves smoothly with the excess energy above the saddle point, unlike previous predictions relevant to the hydrogenic case.[16] Theoretically, Bordas described a semiclassical analysis of this process and presented numerical simulations in excellent agreement with the experimental results.[1] It was shown that the background contribution dominates in the observations. Detailed calculations were carried out by Zhao and

*Project supported by the National Natural Science Foundation of China (Grant No. 10774162).

†Corresponding author. E-mail: liuhongping@wipm.ac.cn

© 2011 Chinese Physical Society and IOP Publishing Ltd

Delos in semiclassical and quantum-mechanical frameworks respectively.[17,18] In our previous work,[19] the photoionization microscopy of a hydrogen atom in parallel electric and magnetic fields was calculated. We found that the two main interference patterns like the case for pure electric field can be identified, meanwhile, new patterns appear resulting from the trajectories encircling the nucleus.

It can be expected that more interesting results will appear if we apply photoionization microscopy to a Rydberg atomic system with more complex interactions such as a Rydberg hydrogen atom near a metal surface. This kind of system can simulate many dynamical effects of atoms in strong fields, such as Zeeman–Stark effect, diamagnetic effect, instantaneous van der Walls interaction, etc.[20] For the atom near a metal surface, the interaction potential has been studied by the method of electric image theoretically[21,22] and has also been verified experimentally.[22−25] For the ionization of molecules at a metal surface, some experimental works have been reported.[26,27] At the same time, many theoretical works have also been done to study the dynamical properties of the Rydberg atoms[28−31] and spectral properties of the atom near a metal surface by quantum method[32,33] and semiclassical method.[20,34−38] Specially, Wang *et al*. applied the closed-orbit theory to the study of the dynamical properties and calculation of the photoabsorption spectra and absorption spectra of Rydberg hydrogen atom[20] and non-hydrogenic atom[34] near a metal surface. Recently, they studied the ionization process in the time domain at different scaled energies above the classical saddle point energy[39] and found that the metal surface can play the role of both the electric and the magnetic fields.

Rather than in time domain, in this paper, we investigate the ionization phenomena of atom near metal surface by microscopy of electron in transverse spatial direction. In time domain, the ionization of atom near metal surface behaves by emitting a train of electron pulses. It gives an equivalent simulation to investigate the effect of strong diamagnetic fields on the ionization dynamics and manifests how the chaos comes to play a role when the "diamagnetic term" predominates.[39] We expect the ionization microscopy of atom near metal surface will exhibit similar behaviour in spatial domain. In the microscopy, the electron waves travel along different classical paths from the ion to the detector and the different trajectories interfere with each other transversely. The interference pattern is recorded by a position-sensitive detector. The image recorded on the detector reflects the distribution of the square modulus of the transverse component of the electronic wave function. In this way, with the recorded interference pattern, we can investigate the general ionization dynamics of atom near metal surface as well as the chaos induced by the non-linear interaction term in the Hamiltonian.

## 2. Theory

Assuming an infinitely massive nucleus at the origin of the coordinate system, a metal plate is kept in the $z = -d$ plane (see Fig. 1(a)). For the photoionization microscopy, a position-sensitive detector is placed between them. The potential experienced by the Rydberg electron is the combination of the Coulomb potential and the electrical image potential induced by the metal surface. We can obtain the latter term by the electric image method. The Hamiltonian for the hydrogen atom near a metal surface has the following form (in cylindrical coordinates and atomic unit)[28]

$$H = \frac{p^2}{2} - \frac{1}{r} + \frac{1}{\sqrt{\rho^2 + (2d+z)^2}} - \frac{1}{4(d+z)}, \quad (1)$$

in which $r = \sqrt{\rho^2 + z^2}$ and $p^2 = p_\rho^2 + l_z^2/\rho + p_z^2$. The last two terms in Eq. (1) are the electrostatic image potential. Owing to the cylindrical symmetry, the $z$-component of angular momentum is conserved and then the $\varphi$-motion can be separated. Thus, in this paper, the system we are interested in is reduced to a problem with two degrees of freedom with $l_z = 0$. After the scaled transformation, $\tilde{r} = r/d$, $\tilde{p} = p\sqrt{d}$ and $\varepsilon = Ed$, dropping the tilde, the classical motion of the electron is governed by the scaled Hamiltonian

$$\begin{aligned}\varepsilon &= \frac{p^2}{2} - \frac{1}{\sqrt{\rho^2 + z^2}} + \frac{1}{\sqrt{\rho^2 + (2+z)^2}} - \frac{1}{4(1+z)} \\ &\equiv \frac{p^2}{2} + U(\rho, z). \end{aligned} \quad (2)$$

According to Eq. (2), the scaled Hamiltonian does not depend on the energy $E$ and the atom–surface distance $d$ separately, but only on the scaled energy $\varepsilon$, thus eliminating the parameter $d$.

It is helpful to study the shape of the effective potential $U(\rho, z)$ in Eq. (2) by determining its saddle points, which are the roots of the equations $\partial U(\rho, z)/\partial z = 0$ and $\partial U(\rho, z)/\partial \rho = 0$. There is only one saddle point: $\rho_s = 0$, $z_s = -0.693673$. As shown in Fig. 1(b), the combination of the Coulomb potential and electrical image potential gives rise to the formation of the saddle point in the potential experienced

by the electron. The point is critical for the calculation. Once the electron passes over the saddle point, it will be ionized and recorded by the detector eventually. In the paper, we place the detector at $z = -0.8$ (scaled unit).

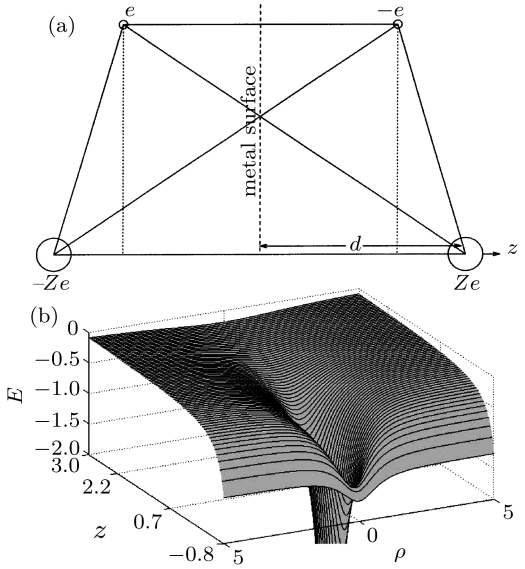



**Fig. 1.** (a) The pictorial representation of an atom and its image near a metal surface located at a distance $d$.[32] (b) Schematic view of the potential energy surface for the atom near a metal surface. Scaled unit is used in panel (b).

In order to integrate the Hamiltonian motion equations, the Coulomb singularity in the Hamiltonian equation (2) has to be removed. For the case considered here, we could make a regularized transformation to semi-parabolic coordinates $(\mu, \nu)$, where $\mu^2 = r+z$, $\nu^2 = r-z$, $p_\mu = \mathrm{d}\mu/\mathrm{d}\tau$, $p_\nu = \mathrm{d}\nu/\mathrm{d}\tau$, with the new scaled time defined as $\mathrm{d}\tau = \mathrm{d}t/(\mu^2+\nu^2)$.[40] Then, we introduce an effective Hamiltonian $h = 2r(H-\varepsilon)$, on which our calculation is based. The new Hamiltonian is defined as

$$\begin{aligned} h(\mu,\nu,p_\mu,p_\nu) = {} & \frac{1}{2}(p_\mu^2+p_\nu^2) - \varepsilon(\mu^2+\nu^2) \\ & + \frac{\mu^2+\nu^2}{\sqrt{\mu^2\nu^2 + \left(2+\dfrac{\mu^2-\nu^2}{2}\right)^2}} \\ & - \frac{\mu^2+\nu^2}{4\left(1+\dfrac{\mu^2-\nu^2}{2}\right)} - 2. \end{aligned} \tag{3}$$

Our treatment is strictly limited to the semiclassical approximation and the contribution of the tunneling is neglected. In the calculation, however, the Maslov index is introduced to correct the phase due to the failure of the semiclassical approximation when the momenta vanish.

Suppose an electron in the excited state is ejected at an angle $\theta$, which is defined as the angle between the initial velocity of the photoelectron and the $z$ axis and arrives at the detector located at $z = z_0$. For the point on the detector surface, denoted by $M(R, z_0)$, there exist an infinite number of photoelectron trajectories passing through it. In the semiclassical approximation, the magnitude and phase of the semiclassical wave function for trajectory $i$, denoted by $\psi_i(R)$, depend on its classical density $\rho_i$ and classical action functional $S_i(R, \varepsilon)$

$$\psi_i(R) = \sqrt{\rho_i(R)}\exp\left(\mathrm{i}\chi_i(R)\right). \tag{4}$$

Here, the phase $\chi_i(R)$ is given by

$$\begin{aligned} \chi_i(R) &= S_i(R,E)\omega - \frac{\pi}{2}\mu_i(i), \\ S_i(R,\varepsilon) &= \int_0^M p_i \mathrm{d}q_i, \end{aligned} \tag{5}$$

where $\omega = \sqrt{d}$ and the Maslov index $\mu_i(R)$, which was not incorporated by Bordas *et al.*,[1] keeps track of the singularity "history" of the trajectory where the density $\rho_i$ diverges.

The procedure of the calculation is similar to our previous paper.[19] For given scaled energy $\varepsilon$ and position of the detector $z_0$, we model the electronic wave function, immediately after the excitation, by an ensemble of classical trajectories that begin at the nucleus and propagate radially outwards in all directions with an isotropic initial electron angular distribution. For a given radius $R$ at the detector, the Hamiltonian (3) is integrated numerically to track the classic trajectory of the electron. If the landing position at the detector is in the vicinity of $R$, the ejected angle $\theta_i(R)$ is recorded and phase $\chi_i(R)$ is calculated according to Eq. (5). We stop the integration if the electron cannot reach the detector within a maximum time $T_0$. In this paper, we have $T_0 = 20$ (scaled unit).

After weighting the contribution of the start direction $\theta$ according to the density $\sin\theta$, the resulting wavefunction $\psi(R)$ at point $M(R, z_0)$ is subsequently obtained by summing the amplitudes over all possible trajectories leading from the electron source to this point according to

$$\begin{aligned} & \psi_{\mathrm{sc}}(R) \\ & = \sum_i \psi_i(R) \\ & = \sum_i \left(\frac{\mathrm{d}\theta_i(R)}{\mathrm{d}R}\sin\theta_i(R)\right)^{1/2} \exp[\mathrm{i}\chi_i(R)], \end{aligned} \tag{6}$$

where $\theta_i$ represents any ejection angle leading to the detection of the electron at radius $R$ on the detector.

The calculated radial probability distribution $\rho_{\rm sc}(R)$ on the detector is then obtained according to

$$\rho_{\rm sc}(R) = |\psi_{\rm sc}(M(R,z_0))|^2 = \sum_i \rho_i + 2\sum_{i<j}\sqrt{\rho_i\rho_j}\cos(\chi_i-\chi_j). \quad (7)$$

The second term in Eq. (7) represents interference among classical paths. We can find that the radial probability distribution is different from their classical counterparts by the presence of interference terms.

Following Mitchell and Delos,[41] we describe the shapes of these trajectories symbolically using a string of dashes and ohs $\{-, o\}$. Each dash represents a portion of the trajectory that begins on the negative $z$ axis and returns to it without encircling the nucleus. Each oh represents a portion that does encircle the nucleus. We record the symbols from left to right, beginning with the first intersection away from the nucleus and ending when the trajectory reaches the detector. If the trajectory does not encircle the nucleus before reaching the detector, we label it "direct" trajectory. Figures 2(a)–2(d) show some typical trajectories and their definitions. For example, figure 2(a) is the direct trajectory, propagating away from the atomic nucleus towards the metal surface. The electron passes over the saddle points and hits the detector without encircling the nucleus. While in Fig. 2(b), the electron crosses the negative $z$ axis and then encircles the nucleus before impacting the detector. The four types of trajectories shown in Fig. 2 are stable and have evident contribution to the interference pattern in our calculation.

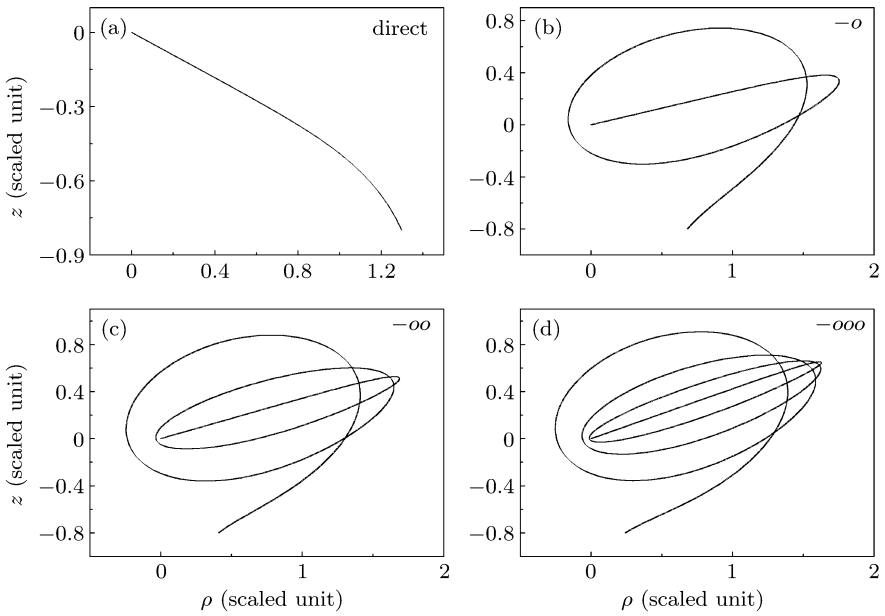



**Fig. 2.** Some typical trajectories for hydrogen atoms near metal surface at scaled energy $\varepsilon = -0.4$. The orbital type is labeled in each panel.

## 3. Result and discussion

The variation of the impact radius $R$ as a function of the ejection angle $\theta$ is illustrated in Fig. 3. There exists a critical angle $\theta_{\rm c}$. If electrons launched at an angle smaller than $\theta_{\rm c}$, they will never escape the Coulomb attraction and cannot reach the detector within the given time $T_0$. An infinite number of trajectories launching at the initial angle $\theta > \theta_{\rm c}$ can impact on the detector. These trajectories can be classified into a few types. The types of trajectories that will emerge and contribute to the interference pattern depend on the scaled energy $\varepsilon$. In Fig. 3(a), for the electrons at an initial angle $\theta > 2$, they move towards the detector, pass through the saddle point and hit the detector without crossing the negative $z$ axis. These trajectories are defined as direct trajectories. In the calculation, the direct trajectories dominantly contribute to the interference patterns. When $\theta$ is around 1.93, the electron crosses the negative $z$ axis and then encircles the nucleus before its second crossing with the negative $z$ axis, finally hitting the detector. This type of trajectories is labeled by $-o$. When the scaled energy $\varepsilon = -0.1$ as depicted in Fig. 3(b), the critical angle $\theta_{\rm c}$ is very small and most of the electrons can find their way to the detector. Two types of indirect trajectories, $-o$ and $-oo$, appear when the launching angle $\theta$ is small. In the calculation, we set the maximal time $T_0 = 20$. If we have a larger $T_0$, we will have

more types of indirect trajectories. The trajectories corresponding to the extremely sharp peaks labeled by stars in Fig. 3 are very unstable and nearly have no effect on the structure of the interference pattern. The difference between Figs. 3(a) and 3(b) can be explained clearly with the potential energy surface of the electron in Fig. 1(b). When $\varepsilon$ is small, the ionization channel is very narrow and only trajectories with large launching angle can reach the detector. When $\varepsilon$ increases to $-0.1$, the ionization channel gets broader and nearly all trajectories can arrive at the detector directly or reflected by the potential and encircle the nucleus at least once.

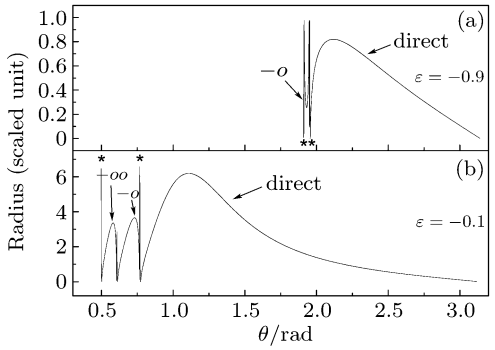



**Fig. 3.** The dependence of the impact radius $R$ of imaging electrons on the ejection angle $\theta$ at different scaled energies, (a) $\varepsilon = -0.9$ and (b) $\varepsilon = -0.1$. The types of the trajectories relevant to the corresponding region are indicated. Electrons launched at an angle smaller than $\theta_c$ can never escape the Coulomb attraction. The sharp peaks labeled by stars correspond to the trajectories extremely unstable and nearly have no effect to the structure of the interference pattern.

In order to have a clear insight into the building up of the interference pattern, the total radial distribution of the electron flux is decomposed into its direct and indirect components as shown in Figs. 4(a)–4(c) with atom–surface distance $d = 1200$ a.u. The electron flux is proportional to the square modulus of the wave function.[1] The radial distribution of total flux, shown in Fig. 4(a), is the coherent superposition of different trajectories' contributions. For the case with $\varepsilon = -0.1$, the launching angles with $\theta > 0.77$ correspond to the contribution of direct electrons (see Fig. 3(b)), giving rise to a clearly beating pattern and a peak at $R = 6.2$ (at which $\mathrm{d}\theta/\mathrm{d}R$ has its maximum), as seen in Fig. 4(b); while the launching angles with $\theta < 0.77$ correspond to the indirect electrons' contribution. There are two types of indirect trajectories contributing to the interference pattern, as shown in Fig. 4(c). As the launching angle $\theta$ for indirect trajectories is small, this will lead to a small $\sin\theta$. Thus, according to Eqs. (6) and (7), the contributions of indirect trajectories are very weak compared to that of direct trajectories. Meanwhile, the phase $\chi_i$ for the indirect trajectories varies very slowly compared to the variation of $\mathrm{d}\theta/\mathrm{d}R$, resulting in that we cannot see clear beating pattern from the contribution of the indirect electrons. A contour plot of electron flux distribution at $\varepsilon = -0.1$ is drawn in Fig. 4(d). It displays the 3D-contour of the radial distribution of the total electron flux in Fig. 4(a) and can be recorded by the position-sensitive detector in the experiment.

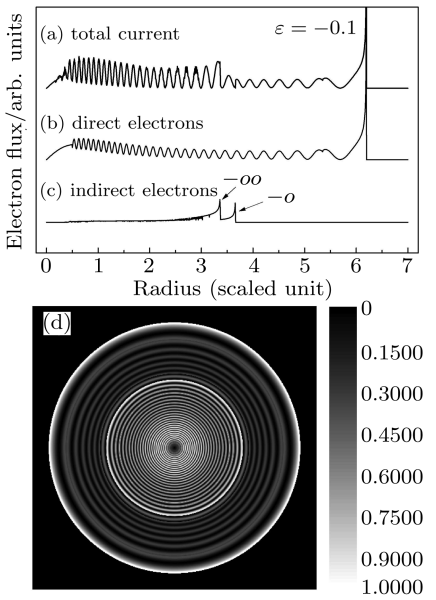



**Fig. 4.** Radial distributions of electron flux on the detector at $\varepsilon = -0.1$, shown in panels (a)–(c). Panel (a) is for the total contribution of direct and indirect electrons; (b) and (c) are for the contributions of direct electrons and indirect electrons, respectively; (d) is the contour plot of the total electron flux distribution (a) in the plane of detector surface.

The radial distribution of the electron flux is dependent on the excitation energy. Figure 5 shows the radial distributions of the electron flux at various scaled energies. The labels 1, 2, and 3 denote the types of trajectories: direct, $-o$ and $-oo$, respectively. The evolutions of most patterns are smooth with increasing scaled energy, as expected for the assumption of an isotropic initial distribution of the ejected angles.[3,16] When the scaled energy is below $\varepsilon = -1.1$, the radial spectrum of the electron flux is dominated by the pattern 1, corresponding to the direct orbital. The contribution of the trajectories $-o$, labeled by 2, begins to take effect at $\varepsilon = -1.1 \approx 0.77\varepsilon_{\mathrm{sp}}$, which is similar to trajectories $-$ in the case of parallel electric and magnetic fields.[19]

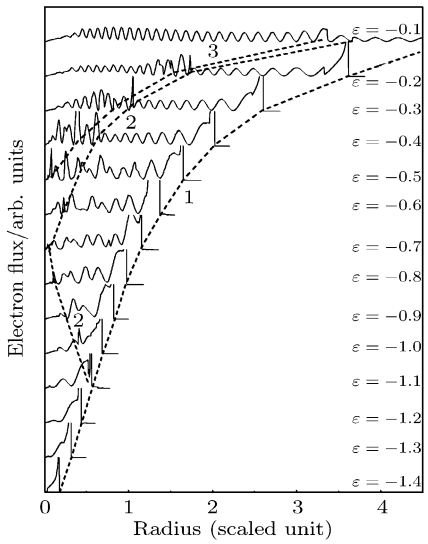



**Fig. 5.** Radial distributions of electron flux at the scaled energies varying between saddle point energy $\varepsilon_{\rm sp} = -1.499$ and $\varepsilon = 0$. The distance between atom and surface is set to $d = 1200$ a.u. The evolutions of radial peaks resulting from the contribution of the same type of trajectories are plotted in dotted line and labeled by numbers 1, 2 and 3 (see text for details).

For the orbit $-o$, the radius of the electrons impacting on the detector decreases smoothly to its minimum at $\varepsilon = -0.7$ and then increases when $\varepsilon$ increases. With the increase of $\varepsilon$, the electrons are more and more easily influenced by the electrostatic image potential. The electrons with smaller ejected angle is strongly deflected by the effective potential. When it comes to $\varepsilon = -0.5$, the trajectories $-oo$ labeled by 3 comes to emerge as seen in Fig. 5. At this moment, the electrons will first cross the negative $z$ axis and then encircle the nucleus twice before hitting the detector. If we have the maximum time $T_0 > 20$, the trajectories encircling the nucleus more times will appear. The emergence of the trajectories encircling nucleus with the increase of $\varepsilon$ is similar to the case of the hydrogen atom in parallel electric and magnetic fields.[19]

Radial distributions of the electron flux at different atom–surface distances are shown in Fig. 6 from which we can investigate the similar "diamagnetic effect" on the radial spectrum. When $d^2 \gg r^2$, retaining only the quadratic terms in the binomial expansions, we can approximate the Hamiltonian of the hydrogen atom near a metal surface, i.e. Eq. (1) by[32]

$$H = \frac{p^2}{2} - \frac{1}{r} + \frac{1}{\sqrt{\rho^2 + (2d+z)^2}} - \frac{1}{4(d+z)} = \frac{p^2}{2} - \frac{1}{r} - \frac{1}{8d^3}z^2 - \frac{1}{16d^3}\rho^2. \quad (8)$$

Examining the last term in Eq. (8), it can be understood as a diamagnetic effect of an external magnetic field.[39] In our case, if we take the principal

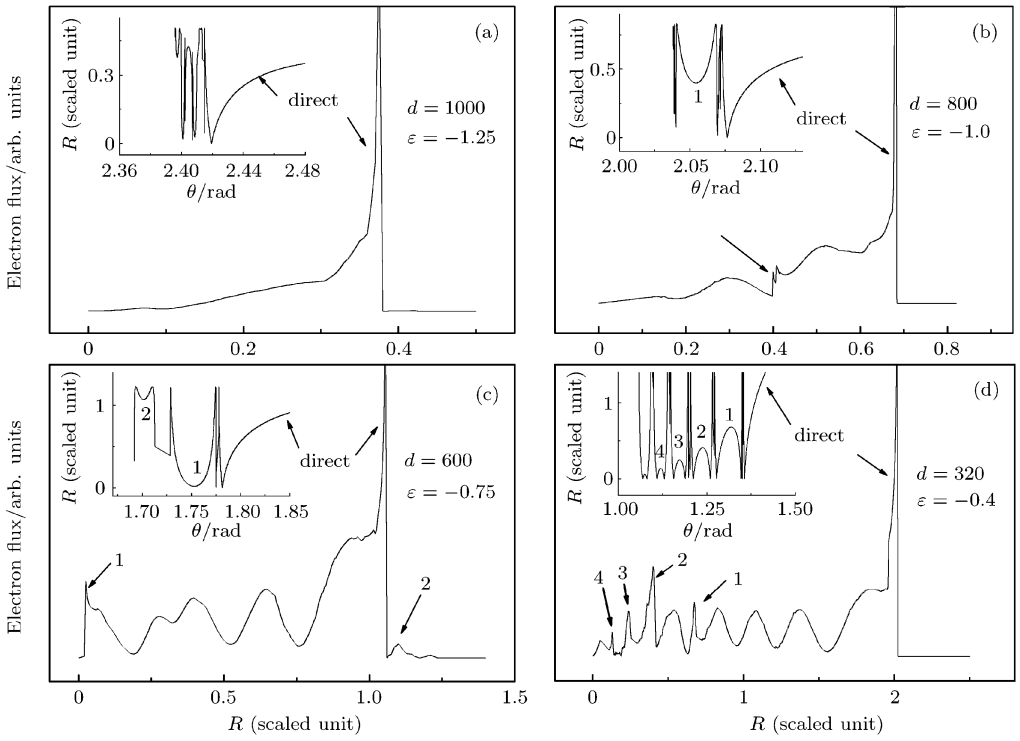



**Fig. 6.** Radial distribution of the electron flux at different atom–surface distance $d$. The variation of the impact radius $R$ as a function of the launching angle $\theta$ is shown in the inset. The integers 1, 2, 3, and 4 represent the types of trajectories $-o$, $-oo$, $-ooo$, $-oooo$, respectively.

quantum number of the final state to be $n = 20$, then the excited state energy will be $E = -1/2n^2 = -1.25 \times 10^{-3}$ a.u. Matching $\varepsilon = Ed$ and $(1/16d^3)\rho^2 = (1/8)\gamma^2\rho^2$, at a given atom–surface distance $d$ (atomic unit), we can obtain the scaled energy $\varepsilon$ and the corresponding equivalent magnetic field $B$. For example, for the various values of $d$ as shown in Fig. 6(a)–6(d), the corresponding magnetic field $B$ is 5.25, 7.34, 11.31, and 29.02 T, respectively. For the case of $d = 1000$ a.u. in Fig. 6(a), the variation of $R$ versus $\theta$ is plotted in the inset. It can be seen that only the direct trajectory is stable and has dominant contribution to the radial distributions of the electron flux, so there is only one evident peak in the radial distribution as shown in the main figures. When the atom–surface distance $d$ decreases to 800 a.u. (equivalent to a magnetic field $B = 5.25$ T), there appears a new trajectory $-o$, which is chaotic due to the "diamagnetic effect", labeled by integer 1 in Fig. 6(b). When $d = 600$ a.u., corresponding to $B = 11.31$ T, more chaotic trajectories, such as $-o$, $-oo$, appear, as labeled with 1 and 2, respectively in Fig. 6(c). When the atom–surface distance $d$ decreases down to 320 a.u. (equivalent to $B = 29.02$ T), the diamagnetic effect term is strong enough to make the system deeply chaotic. The trajectory encircling nucleus up to four times appears, labeled by integer 4 as shown in Fig. 6(d). Thus, with increasing scaled energy $\varepsilon$ and decreasing atom–surface distance $d$, more complicated trajectories appear and the interference patterns get more complex, which is a manifest of the classical chaos. Then, we can draw the similar conclusion in the spatial domain like the case in time domain, in which the classical chaos is manifested by the existence of pulse trains.[39]

# 4. Conclusion

We have performed a theoretical calculation of the ionization microscopy of the hydrogen atom near a metal surface. The results show that different types of trajectories contribute predominantly to different manifold in a certain interference pattern. With the increase of the scaled energy or the decrease of the atom–surface distance, more indirect trajectories will emerge, accompanied by classical chaos. Therefore atom near a metal surface is a good simulation system to investigate the strong diamagnetic effect that is not available in real laboratory magnetic field. The calculation also shows that the ionization of atom near the metal surface has a similar spectral structure in spatial domain, as the case of ionization of atom in parallel electric and magnetic fields. The calculation is based on the approximation that electrons are ejected isotropically in all directions, implying that only the so-called background contribution is considered. This approximation is rational as the chaos can be induced by the diamagnetic effect term generated by the metal surface.

# References


[1] Bordas C, Lépine F, Nicole C and Vrakking M J J 2003 *Phys. Rev. A* **68** 012709

[2] Demkov Y, Kondratovich V and Ostrovskii V 1982 *JETP Lett.* **34** 403

[3] Kondratovich V D and Ostrovsky V N 1984 *J. Phys.* B **17** 1981

[4] Kondratovich V D and Ostrovsky V N 1984 *J. Phys.* B **17** 2011

[5] Blondel C, Delsart C and Dulieu F 1996 *Phys. Rev. Lett.* **77** 3755

[6] Blondel C, Delsart C, Dulieu F and Valli C 1999 *Eur. Phys. J.* D **5** 207

[7] Kramer T, Bracher C and Kleber M 2002 *J. Phys.* A **35** 8361

[8] Du M L 1989 *Phys. Rev.* A **40** 4983

[9] Kramer T, Bracher C and Kleber M 2001 *Europhys. Lett.* **56** 471

[10] Bracher C, Kramer T and Delos J B 2006 *Phys. Rev.* A **73** 062114

[11] Bracher C and Delos J B 2006 *Phys. Rev. Lett.* **96** 100404

[12] Bordas C 1998 *Phys. Rev.* A **58** 400

[13] Lépine F, Bordas C, Nicole C and Vrakking M J J 2004 *Phys. Rev.* A **70** 033417

[14] Nicole C, Offerhaus H L, Vrakking M J J, Lépine F and Bordas C 2002 *Phys. Rev. Lett.* **88** 133001

[15] Nicole C, Sluimer I, Rosca-Pruna F, Warntjes M, Vrakking M, Bordas C, Texier F and Robicheaux F 2000 *Phys. Rev. Lett.* **85** 4024

[16] Kondratovich V D and Ostrovsky V N 1990 *J. Phys.* B **23** 3785

[17] Zhao L B and Delos J B 2010 *Phys. Rev.* A **81** 053417

[18] Zhao L B and Delos J B 2010 *Phys. Rev.* A **81** 053418

[19] Wang L, Yang H F, Liu X J, Liu H P, Zhan M S and Delos J B 2010 *Phys. Rev.* A **82** 022514

[20] Wang D, Du M L and Lin S 2006 *J. Phys.* B **39** 3529

[21] Zaremba E and Kohn W 1976 *Phys. Rev.* B **13** 2270

[22] Fabre C, Gross M, Raimond J M and Haroche S 1983 *J. Phys.* B **16** L671

[23] Shih A, Raskin D and Kusch P 1974 *Phys. Rev.* A **9** 652

[24] Anderson A, Haroche S, Hinds E A, Jhe W and Meschede D 1988 *Phys. Rev.* A **37** 3594

[25] Sandoghdar V, Sukenik C I, Hinds E A and Haroche S 1992 *Phys. Rev. Lett.* **68** 3432
[26] Lloyd G R, Procter S R and Softley T P 2005 *Phys. Rev. Lett.* **95** 133202
[27] Lloyd G R, Procter S R, McCormack E A and Softley T P 2007 *J. Chem. Phys.* **126** 184702
[28] Simonovic N S 1997 *J. Phys.* B **30** L613
[29] Ge M, Zhang Y, Wang D, Du M and Lin S 2005 *Sci. Chin.* G **48** 667
[30] Inarrea M, Lanchares V, Palacian J F, Pascual A I, Salas J P and Yanguas P 2007 *Phys. Rev.* A **76** 052903
[31] Wang L, Yang H F, Liu X J and Liu H P 2010 *Chin. Phys.* B **19** 113301
[32] Ganesan K and Taylor K T 1996 *J. Phys.* B **29** 1293
[33] Nordlander P 1996 *Phys. Rev.* B **53** 4125
[34] Wang D H 2008 *Commun. Theor. Phys.* **49** 467
[35] Li H Y, Zhao X, Gao S, Xu X Y, Zhou H and Lin S L 2008 *Eur. Phys. J.* D **49** 1
[36] Wang D H 2009 *Commun. Theor. Phys.* **51** 310
[37] Huang K Y and Wang D H 2010 *Chin. Phys.* B **19** 063402
[38] Li H Y, Gao S, Zhou H, Zhang Y H and Lin S L 2008 *Chin. Phys.* B **17** 2932
[39] Wang D, Huang K and Lin S 2009 *Eur. Phys. J.* D **54** 699
[40] Main J, Wiebusch G, Welge K, Shaw J and Delos J B 1994 *Phys. Rev.* A **49** 847
[41] Mitchell K and Delos J 2007 *Physica* D **229** 9